

Magneto-gyrotropic photogalvanic effect and spin dephasing in (110)-grown GaAs/AlGaAs quantum well structures

P. Olbrich¹, J. Allerdings¹, V.V. Bel'kov^{1,2}, S.A. Tarasenko², D. Schuh¹,
W. Wegscheider¹, T. Korn¹, C. Schüller¹, D. Weiss¹, and S.D. Ganichev¹

¹*Terahertz Center, University of Regensburg, 93040 Regensburg, Germany and*

²*A.F. Ioffe Physical-Technical Institute, Russian Academy of Sciences, 194021 St. Petersburg, Russia*

We report on the magneto-gyrotropic photogalvanic effect (MPGE) in *n*-doped (110)-grown GaAs/AlGaAs quantum-well (QW) structures caused by free-carrier absorption of terahertz radiation in the presence of a magnetic field. The photocurrent behavior upon variation of the radiation polarization state, magnetic field orientation and temperature is studied. The developed theory of MPGE describes well all experimental results. It is demonstrated that the structure inversion asymmetry can be controllably tuned to zero by variation of the delta-doping layer positions. For the in-plane magnetic field the photocurrent is only observed in asymmetric structures but vanishes in symmetrically doped QWs. Applying time-resolved Kerr rotation and polarized luminescence we investigate the spin relaxation in QWs for various excitation levels. Our data confirm that in symmetrically doped QWs the spin relaxation time is maximal, therefore, these structures set the upper limit of spin dephasing in GaAs/AlGaAs QWs.

PACS numbers: 73.21.Fg, 72.25.Fe, 78.67.De, 73.63.Hs

I. INTRODUCTION

Zincblende-structure-based quantum wells (QWs) grown on (110)-oriented substrates recently attracted considerable attention. The particular feature of such structures is their extraordinarily slow spin dephasing, being of importance for spin transport in spintronic devices^{1,2,3,4}. The reason for the long spin lifetime of several nanoseconds even at room temperature is the suppression of the D'yakonov-Perel' mechanism of spin relaxation in symmetrical (110)-grown heterostructures.⁵ In QWs of such crystallographic orientation, the effective magnetic field induced by the bulk inversion asymmetry (BIA) points along the growth axis and, therefore, does not lead to the relaxation of spins oriented along this direction. However, in asymmetrical structures, where the structure inversion asymmetry (SIA) is present, Rashba spin-orbit coupling (for review see^{6,7,8}) induces an in-plane effective magnetic field, thus speeding-up spin dephasing. Experimental access to the symmetry, spin splitting of the band structure, etc., is provided by the magneto-gyrotropic photogalvanic effect (MPGE)^{9,10}. The MPGE stands for a photocurrent generation which requires simultaneously gyrotropy and the presence of a magnetic field.^{10,11,12} The gyrotropic point group symmetry makes no difference between components of axial and polar vectors, and hence allows an electric current $j_\alpha \propto IB_\beta$, where I is the light intensity inside the sample and B_β are components of the applied magnetic field. The microscopic model of the MPGE is based on the asymmetry of photoexcitation and/or relaxation processes in low-dimensional systems with bulk or structure inversion asymmetries^{13,14}.

In this paper, we present an experimental and theoretical study of the MPGE induced by Drude absorption of terahertz (THz) radiation in GaAs/AlGaAs QWs grown on (110)-oriented substrates. In contrast to interband op-

tical transitions, here we deal with monopolar currents because only one type of carriers, conduction electrons, are involved in the photoexcitation. The paper is organized as following. In Sec. II, the macroscopic features of the magneto-gyrotropic effect, e.g., the possibility to generate a photocurrent in various experimental geometries and its behavior upon variation of the radiation polarization, are described in the frame of the phenomenological theory. In Sections III and IV, we give a short account of the experimental technique, present the experimental results on the photocurrents and discuss them in view of the theoretical background. Here, we also discuss applications of the MPGE, in particular, for the study of BIA and SIA responsible for the spin splitting of subbands in *k*-space. Preliminary results on the study of BIA and SIA are published in Ref. [9]. In Sec. V, the experimental data on spin relaxation obtained by means of time-resolved Kerr rotation and polarized luminescence are discussed and compared with the MPGE data. Finally, in Sec. VI we present a short account on magnetic field independent linear and circular photogalvanic currents, which can also be generated in (110)-grown QWs at normal incidence and should be taken into account in studying the MPGE.

II. PHENOMENOLOGICAL THEORY

The phenomenological theory of magneto-gyrotropic effects describes dependencies of the photocurrent magnitude and direction on the radiation polarization state and the orientation of the magnetic field with respect to the crystallographic axes. This theory operates with measurable physical quantities, such as electric current, magnetic field, and light polarization, and does not require a knowledge of the microscopic mechanisms involved.

Within linear approximation in the magnetic field

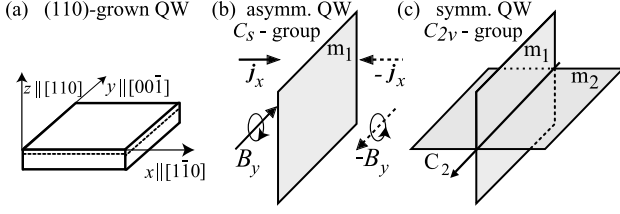


FIG. 1: (a) Coordinate system together with sample sketch, (b) and (c) mirror planes in asymmetrical and symmetrical QW grown along $z \parallel [110]$, respectively. Arrows in the drawing (b) show that the reflection in the plane m_1 changes the sign of both polar vector component j_x and axial vector component B_y , demonstrating that the linear coupling $j_x \propto B_y$ is allowed in asymmetrical QWs. In symmetrical QWs [sketch (c)], the linear coupling of the in-plane current and the in-plane magnetic field is forbidden because the reflection in the plane m_2 does not modify \mathbf{j} but changes the sign of the in-plane components of the axial vector \mathbf{B} .

strength \mathbf{B} , the MPGE at normal incidence is described by¹⁵

$$j_\alpha^{\text{MPGE}} = \sum_{\beta\gamma\delta} \phi_{\alpha\beta\gamma\delta} B_\beta I \frac{(e_\gamma e_\delta^* + e_\delta e_\gamma^*)}{2} \quad (1)$$

$$+ \sum_{\beta\gamma} \mu_{\alpha\beta\gamma} B_\beta \hat{e}_\gamma IP_{\text{circ}},$$

where ϕ is a fourth rank pseudo-tensor being symmetric in the last two indices, $\mathbf{e} = \mathbf{E}/|\mathbf{E}|$ is the (complex) unit vector of the light polarization, \mathbf{E} is the radiation electric field, $\hat{\mathbf{e}}$ is the unit vector pointing in the light propagation direction and P_{circ} is the radiation circular polarization degree. The pseudo-tensor ϕ describes photocurrents which can be induced by linearly polarized or unpolarized radiation while $\mu_{\alpha\beta\gamma}$ stands for the light helicity dependent photocurrent which reverses its direction upon switching the sign of the circular polarization.

As in the experiment described below, we consider zinc-blend structure based quantum wells grown on (110)-oriented substrates and normal incidence of the light. Depending on the equivalence or non-equivalence of the QW interfaces, the structure symmetry may belong to one of the point groups: C_{2v} or C_s , respectively.¹⁶ The symmetry elements of symmetrical and asymmetrical QWs are shown in Fig. 1, where the coordinate frame with the in-plane axes $x \parallel [110]$ and $y \parallel [001]$, and the growth direction $z \parallel [110]$ is used for convenience.

The phenomenological equation (1) shows that the photocurrent can only occur for those components of the field \mathbf{B} and polarization vector \mathbf{e} whose products transform as the in-plane components of \mathbf{j} for all symmetry operations. Let us consider it for unpolarized radiation. In this particular case, the photocurrent is determined solely by the coupling of the polar vector \mathbf{j} to the axial vector \mathbf{B} because $(e_\gamma e_\delta^* + e_\delta e_\gamma^*) = \delta_{\gamma,\delta}$ becomes an invariant and $P_{\text{circ}} = 0$. In the asymmetric structures

(C_s point group) the only symmetry element, apart from identity, is the reflection plane m_1 normal to the x axis. The reflection in m_1 transforms the current component j_x and the magnetic field component B_y the same way ($j_x \rightarrow -j_x$, $B_y \rightarrow -B_y$), see Fig. 1b. Therefore, the coupling $j_x \propto B_y$ is allowed. The same arguments hold for $j_y \propto B_x$ and $j_x \propto B_z$. As a result, the generation of a magnetic field-induced photocurrent is possible for both, in-plane and out-of-plane magnetic fields. Symmetric (110)-grown QWs, which belong to the higher point-group symmetry C_{2v} , contain an additional mirror plane m_2 being parallel to the interface plane, see Fig. 1c. The reflection in m_2 does not modify the in-plane components of the polar vector \mathbf{j} but changes the polarity of the in-plane components of the axial vector \mathbf{B} . Therefore, a linear coupling of the current and the in-plane magnetic field is forbidden. The coupling of j_x and B_z , however, is allowed for reflections in both m_1 and m_2 planes demonstrating that a photocurrent j_x can be induced in the presence of a magnetic field B_z , even in symmetric (110)-oriented QWs. This analysis shows that the MPGE is an ideal tool to probe the symmetry of (110)-grown QWs. For in-plane magnetic field, the photocurrent can only be observed in asymmetric structures but vanishes if the QWs are symmetric.

For polarized radiation the phenomenological theory should also take into account components of the polarization vector. This results in additional polarization dependent contributions to the photocurrent. Below we present results of such an analysis of the MPGE describing the polarization dependence of the photocurrent for symmetrical and asymmetrical structures.

A. Asymmetrical structures, C_s point group

In asymmetrical structures, the MPGE induced by normally-incident linearly-polarized light is generally described by 9 linearly independent constants $S_1 \dots S_9$, see Table I:

$$j_x^{\text{MPGE}}/I = S_1 B_y + S_2 B_y (|e_x|^2 - |e_y|^2) \quad (2)$$

$$+ S_3 B_x (e_x e_y^* + e_y e_x^*) + S_4 B_z + S_5 B_z (|e_x|^2 - |e_y|^2),$$

$$j_y^{\text{MPGE}}/I = S_6 B_x + S_7 B_x (|e_x|^2 - |e_y|^2)$$

$$+ S_8 B_y (e_x e_y^* + e_y e_x^*) + S_9 B_z (e_x e_y^* + e_y e_x^*).$$

The polarization dependence of the photocurrent is given by

$$|e_x|^2 - |e_y|^2 = \cos 2\alpha, \quad e_x e_y^* + e_y e_x^* = \sin 2\alpha, \quad (3)$$

, where α is the angle between the plane of linear polarization and the x axis. We note that the first terms on the right-hand side of both Eqs. (2) do not depend

$S_1 = \frac{1}{2}(\phi_{xyxx} + \phi_{xyyy})$	$S_2 = \frac{1}{2}(\phi_{xyxx} - \phi_{xyyy})$
$S_3 = \phi_{xxxy} = \phi_{xyyx}$	$S_4 = \frac{1}{2}(\phi_{xxzx} + \phi_{xzyy})$
$S_5 = \frac{1}{2}(\phi_{xxzx} - \phi_{xzyy})$	$S_6 = \frac{1}{2}(\phi_{yxxx} + \phi_{yxyy})$
$S_7 = \frac{1}{2}(\phi_{yxxx} - \phi_{yxyy})$	$S_8 = \phi_{yyxy} = \phi_{yyyx}$
$S_9 = \phi_{yzxy} = \phi_{yzyx}$	$S_{10} = \mu_{xxz}$
$S_{11} = \mu_{yyz}$	$S_{12} = \mu_{yzz}$

TABLE I: Definition of the parameters S_i ($i = 1 \dots 9$) in Eqs. (2) and (4) in terms of non-zero components of the tensors ϕ and μ for asymmetric (110)-grown QWs. Normal incidence of radiation along the z axis is assumed.

on the radiation polarization and describe the currents generated by unpolarized light.

The magnetic field-induced photocurrent can also be excited by elliptically or circularly polarized radiation. In this case, Eqs. (2) remain valid and describe the current independent of the sign of circular polarization. The radiation helicity, however, gives rise to additional current contributions given by

$$\begin{aligned} j_x^{\text{MPGE, circ}}/I &= S_{10}B_xP_{\text{circ}}, \\ j_y^{\text{MPGE, circ}}/I &= S_{11}B_yP_{\text{circ}} + S_{12}B_zP_{\text{circ}}. \end{aligned} \quad (4)$$

In the experiments, elliptically and, in particular, circularly polarized radiation is achieved by passing the laser radiation, initially linearly polarized, e.g., along the x axis, through a $\lambda/4$ -plate. The rotation of the plate results in a variation of both linear and circular polarizations as follows

$$P_{\text{lin}} \equiv (e_x e_y^* + e_y e_x^*) = \frac{1}{2} \sin 4\varphi, \quad (5)$$

$$P'_{\text{lin}} \equiv (|e_x|^2 - |e_y|^2) = \frac{1 + \cos 4\varphi}{2}, \quad (6)$$

$$P_{\text{circ}} = \sin 2\varphi, \quad (7)$$

where φ is the angle between the optical axis of the $\lambda/4$ plate and the direction of the initial polarization. Two Stokes parameters P_{lin} and P'_{lin} describe the degrees of linear polarization along the bisector (xy) and the x axis, respectively, and vanish if the radiation is circularly polarized. The third Stokes parameter P_{circ} describes the radiation helicity. It is zero for linearly polarized radiation and reaches ± 1 for left- or right-handed circular polarization.

B. Symmetrical structures, C_{2v} point group

As addressed above, in (110)-grown structures with equivalent interfaces, one of the two mirror planes lies in the QW plane. A reflection in this mirror plane does not modify the in-plane components of polar vectors (e_x , e_y , j_x , j_y) and the out-of-plane component of axial vectors (B_z), but changes the sign of in-plane components

of axial vectors (B_x , B_y). Therefore, in symmetrical (110)-oriented QW structures, the MPGE induced by normally-incident light is described by Eqs. (2) together with Eqs. (4), where $S_1, S_2, S_3, S_6, S_7, S_8, S_{10}, S_{11} = 0$, i.e. by

$$\begin{aligned} j_x^{\text{MPGE}}/I &= S_4B_z + S_5B_z(|e_x|^2 - |e_y|^2), \\ j_y^{\text{MPGE}}/I &= S_9B_z(e_x e_y^* + e_y e_x^*) + S_{12}B_zP_{\text{circ}}. \end{aligned} \quad (8)$$

C. Linear and circular photogalvanic effects in (110)-grown QWs

Due to the specific crystallographic orientation of (110)-grown QWs, photogalvanic currents at normal incidence of radiation are allowed even at zero magnetic field. They comprise the linear and the circular photogalvanic effect. For normal incidence of the radiation, the photocurrents are given by¹¹

$$\begin{aligned} j_x^{\text{PGE}}/I &= C_1(e_x e_y^* + e_y e_x^*) + C_2P_{\text{circ}}, \\ j_y^{\text{PGE}}/I &= C_3 + C_4(|e_x|^2 - |e_y|^2), \end{aligned} \quad (9)$$

where the parameters C_1 , C_3 , and C_4 describe the linear photogalvanic effect, while C_2 stands for the circular photocurrent, which reverses its direction upon switching the light helicity sign. From Eq. (9) follows that the excitation with unpolarized light in the absence of a magnetic field can lead to an electric current along the y axis only. We note that oblique incidence gives additional roots to photogalvanic effects and may also cause the linear and circular photon drag effect¹⁷.

III. EXPERIMENTAL AND SAMPLES

Magnetic field-induced photocurrents in our experiments were induced by indirect *intra*-subband (Drude-like) optical transitions in the lowest size-quantized subband. We used for optical excitation the emission from a terahertz (THz) molecular laser, optically pumped by a TEA CO₂ laser¹². With NH₃ as active gas, 100 ns pulses of linearly polarized or unpolarized radiation with peak power ~ 10 kW are obtained at wavelengths $\lambda = 90$, 148 and 280 μm (corresponding photon energies $\hbar\omega$ are 13.7 meV, 8.4 meV and 4.4 meV). The terahertz radiation induces free carrier absorption in the lowest conduction subband $e1$ because the photon energies are smaller than the subband separation and much larger than the \mathbf{k} -linear spin splitting. The samples were irradiated along the growth direction.

The experiments here are carried out on molecular-beam epitaxy (110)-grown Si- δ -doped n -type GaAs/Al_{0.3}Ga_{0.7}As structures. The mobility μ and carrier density n_s measured in the dark at 4.2 K are between 0.8×10^5 and 2×10^5 cm²/Vs and between 10^{11} cm⁻² and 10^{12} cm⁻², respectively. The conduction-band profiles of the investigated structures

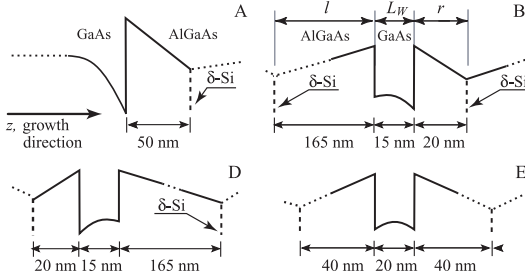


FIG. 2: Band profile of QWs and doping position.

together with the corresponding δ -doping positions and QW widths L_W are shown in Fig. 2. The structures essentially differ in their doping profile: Sample A is a single heterojunction and has the strongest asymmetry, stemming from the triangular confinement potential. In samples B and D, the doping layers are asymmetrically shifted off the QW center either to the left or to the right, respectively. This asymmetric doping yields an asymmetric potential profile inside the QWs (see Fig. 2). All QW structures have 10 QWs. A detailed sample description can be found in Ref. [9]. Sample E was grown fully symmetric containing Si- δ -sheets, placed in the center of each barrier between adjacent QWs. Samples grown along $z \parallel [110]$ were square shaped with the sample edges of 5 mm length oriented along $x \parallel [1\bar{1}0]$ and $y \parallel [00\bar{1}]$. To measure photocurrents, ohmic contacts were alloyed in the center of each sample edge. The MPGE was investigated at room temperature and at low temperatures in an optical cryostat, which allowed the variation of the temperature in a range of 4.2 K to 293 K.

An external magnetic field is applied using a conventional electromagnet either in plane, parallel to y , or normal to the QW plane. The field was varied from $B = -0.8$ T to $B = 0.8$ T. The geometry of the experiment is sketched in the inset of Fig. 3. The photocurrent is measured in unbiased structures via the voltage drop across a 50 Ω load resistor and recorded with a storage oscilloscope. In the experiments, the plane of polarization of the radiation, incident on the sample, was rotated by applying $\lambda/2$ plates, which enabled us to vary the azimuthal angle α from 0° to 180° covering all possible orientations of the electric field vector in the QW plane. To obtain an unpolarized radiation we used a brass cone of 150 mm length with an angle of 4° , to depolarize the radiation due to multiple reflections in the cone.

The spin dynamics in the samples is investigated by means of time-resolved Kerr rotation (TRKR). Here, a circularly polarized pump pulse excites spin-polarized electron-hole pairs within the QWs. A weaker, time-delayed probe pulse tracks the nonequilibrium spin polarization within the sample via the polar magneto-optic Kerr effect: if there is a spin polarization normal to the sample plane, the polarization axis of the reflected light beam will be tilted by a small angle proportional

to the spin polarization. For these measurements, the samples are mounted on the cold finger of a He flow cryostat with optical access, allowing for sample temperatures between 4 K and room temperature. A pulsed Ti-Sapphire laser system generating 600 fs pulses is used for excitation and probing. The central wavelength of the laser is tuned above the absorption onset of the QW to excite electrons slightly above the Fermi energy. For temperature-dependent measurements, this means that the laser wavelength has to be adjusted in order to follow the temperature-dependent absorption onset of the QWs. The laser pulse train is split at a beam splitter, and one part of the pulse train is delayed with respect to the other via a mechanical delay line. An achromatic quarter-wave plate is used to circularly polarize the pump beam, the time-delayed probe beam is linearly polarized. Pump and probe beams are focused onto the sample surface at near-normal incidence with an achromat, resulting in a laser spot size of about 80 μm . The Kerr rotation of the reflected probe beam is analyzed using an optical bridge detector, and this signal is measured as a function of the delay between the pump and probe pulses. The pump beam is modulated with a flywheel chopper, and lock-in detection of the Kerr signal is used to increase the sensitivity. In order to study the photocarrier dynamics in our samples, time-resolved photoluminescence (TRPL) measurements were performed. In these measurements, the sample is non-resonantly excited well above the Fermi energy by the same Ti-Sapphire laser system used for the TRKR measurements. The excitation density is 130 W/cm². The PL emitted from the sample is collected by an achromat and analyzed by a Hamamatsu streak camera system, synchronized to the Ti-Sapphire laser. In order to evaluate the time-resolved PL data, the time-resolved spectra are averaged over a spectral window of 40 meV, centered around the maximum of the PL emission from the QWs. For temperature-dependent measurements, this window is accordingly shifted to lower energy as the PL energy decreases.

IV. EXPERIMENTAL RESULTS

Irradiating samples A, B and D by unpolarized radiation at normal incidence we observe a photocurrent perpendicular to the in-plane magnetic field \mathbf{B} (transverse geometry). The photocurrent pulses duration is about 100 ns, which corresponds to the terahertz laser pulses length. Figure 3 shows the magnetic field dependence of the photocurrent, detected in the GaAs/AlGaAs heterojunction (Sample A). The photocurrent is proportional to the magnetic field strength and its sign depends on the magnetic field direction. The MPGE current has also been detected applying linearly or circularly polarized radiation, but now also in direction along \mathbf{B} (longitudinal geometry). All these results are in agreement with Eqs. (2) for QWs with broken structure inversion. For

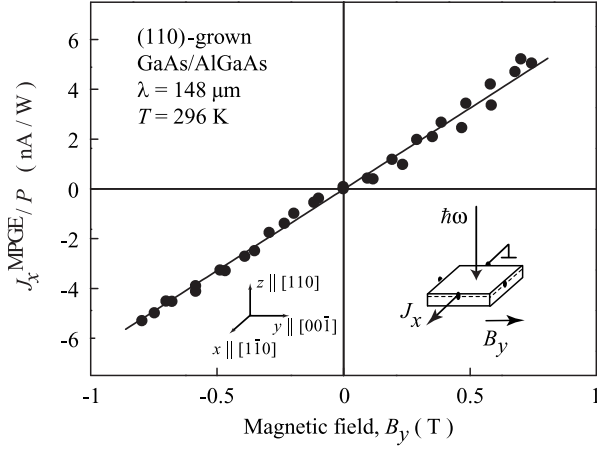


FIG. 3: Magnetic field dependence of the photocurrent measured in (110)-grown GaAs/AlGaAs heterojunction at room temperature with the magnetic field \mathbf{B} parallel to the y axis. Data are obtained for normally incident unpolarized radiation of $P \sim 25$ kW at wavelength $\lambda = 148$ μm .

sample E we do not observe any photocurrent as it is expected for fully symmetric QWs, which do not have structural inversion asymmetry. Recently, we demonstrated that QWs in the symmetrically doped sample E are indeed symmetrical due to the low growth temperature used for preparation of (110)-oriented GaAs structures, which suppress the segregation process⁹.

The illumination of samples A, B and D with linearly or circularly polarized radiation results in a photocurrent even for zero magnetic field. These currents are due to the linear and circular photogalvanic effects and will be considered in Sec. VI. As our experiments here are focused on the MPGE, we eliminate the background by

$$J^{\text{MPGE}} = [J(\mathbf{B}) - J(-\mathbf{B})]/2. \quad (10)$$

We note that in the theoretical parts of the paper the current density \mathbf{j}^{MPGE} is used while in experiment the electric current \mathbf{J}^{MPGE} is measured which is proportional to the current density \mathbf{j}^{MPGE} .

For polarized radiation, the photocurrent is observed in both perpendicular (transverse geometry, Figs. 4a and 5a) and parallel (longitudinal geometry, Figs. 4b and 5b) to the magnetic field \mathbf{B} . The results obtained for $\lambda = 90$ μm , $\lambda = 148$ μm and $\lambda = 280$ μm are qualitatively the same. Therefore, we present only data obtained for $\lambda = 148$ μm . As discussed above, the contributions are characterized by different dependencies of the photocurrent magnitude and direction on the radiation polarization state and the orientation of the magnetic field with respect to the crystallographic axes. As a consequence, a proper choice of the experimental geometry allows one to investigate each contribution separately.

Figure 4 shows the dependence of the photocurrent strength on the orientation of the polarization plane of linearly polarized radiation, given by the angle α for both geometries. The data are presented for a single hetero-

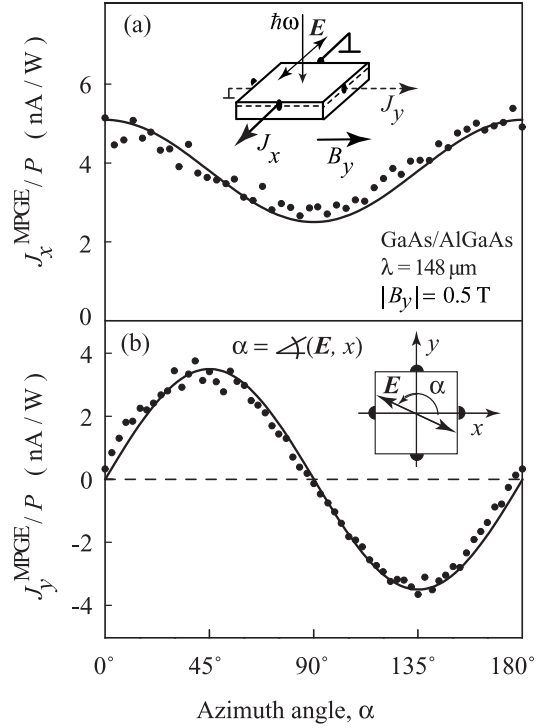


FIG. 4: MPGE photocurrent as a function of angle α measured along (a) x and (b) y axes for magnetic field applied in y -direction. Photocurrent is excited by linearly polarized radiation with wavelength $\lambda = 148$ μm and power $P \sim 5$ kW. Full lines are fits to Eqs. (2). The inset shows the experimental geometry. An additional inset in the lower panel displays the sample and the radiation polarization viewing from the source of radiation side.

junction (sample A) which is single-side doped and belongs to the point group C_s . From Fig. 4 we can clearly see that J_x is proportional to $\cos 2\alpha$ and J_y is proportional to $\sin 2\alpha$. According to Eqs. (2) three photocurrent contributions proportional to S_1 , S_2 and S_8 are allowed in this configuration. The first contribution in the transverse geometry is the same as the one detected for unpolarized radiation which has the same intensity. Two other contributions are proportional to $IB_y \cos 2\alpha$ and $IB_y \sin 2\alpha$ for the transverse photocurrent J_x and the longitudinal photocurrent J_y , respectively, in full agreement with the experiments in Fig. 4.

Applying elliptically polarized radiation we also observed a magnetic field induced photocurrent. The dependence of J^{MPGE} as a function of the angle φ is shown in Fig. 5 for sample A. The data for transverse geometry shown in Fig. 5a can be well fitted by Eqs. (2) taken into account Eqs. (5) and (6). We note that the curves are fitted with the same values of S_1 , S_2 , and S_8 as we used to describe the experiments with linearly polarized radiation. In longitudinal geometry, however, *elliptically* polarized light yields an additional helicity dependent current in agreement with Eqs. (4) containing the term proportional to parameter S_{11} and radiation helic-

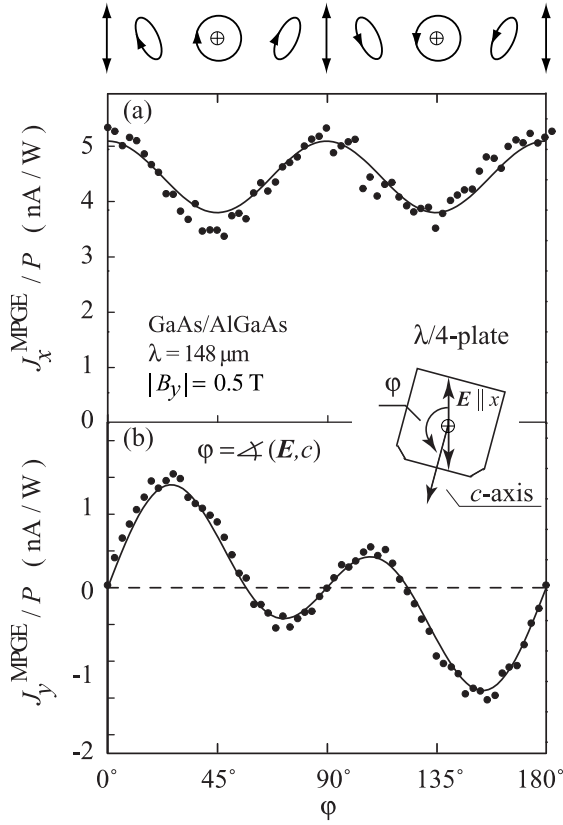


FIG. 5: MPGE photocurrent as a function of angle φ measured along (a) x and (b) y axes for magnetic field applied in y direction. Photocurrent is excited by elliptically polarized radiation with wavelength $\lambda = 148 \mu\text{m}$ and power $P \sim 5 \text{ kW}$. The ellipticity of the radiation is varied by passing linearly polarized laser radiation through a quarter-wave plate (see inset). Full lines are fits of the photocurrent to the sum of Eqs. (2) and (4) with corresponding polarization dependence given by Eqs. (5) - (7). On top, the polarization ellipses corresponding to various phase angles φ are plotted.

ity P_{circ} . While the photocurrent contributions described by S_2 and S_8 result in a current for linear or elliptical polarization, the photocurrent described by the coefficient S_{11} vanishes for linear polarization and assumes its maximum at circular polarization. The polarity of this photocurrent changes upon reversal of the applied magnetic field as well as by changing the helicity from right- to left-handed. The polarization behavior of the current is well described by $j_y \propto IB_y P_{\text{circ}}$. So far a magnetic-field induced photocurrent proportional to P_{circ} has been observed for (001)-grown QWs. It is caused by spin-galvanic effect¹⁸ generated by the optical orientation of carriers, subsequent Larmor precession of oriented electronic spins and asymmetric spin relaxation processes. Though, in general, the spin-galvanic current does not require the application of a magnetic field, it may be considered as a magneto-photogalvanic effect under the above experimental conditions.

The experiment displayed in Fig. 6 (samples A to E)

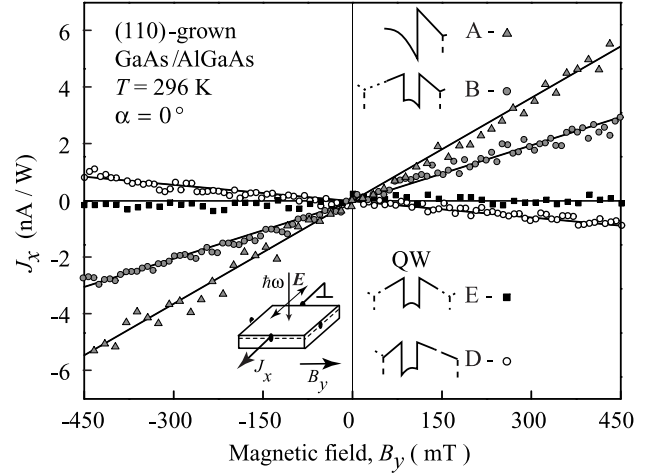


FIG. 6: Magnetic field dependences of the photocurrents measured in x -direction for the radiation polarized along x and the in-plane magnetic field $\mathbf{B} \parallel y$. The magnetic field independent background (see Sec. VI) is subtracted. The left inset shows the experimental geometry. Four right insets show the band profile and the δ -doping position of the investigated samples.

shows that the magnitude of the $J(B_y)$ -slope strongly depends on the doping profile. Furthermore, if the doping layers are asymmetrically shifted off the barrier center from the left to the right side of QWs (from sample B to D, see Fig. 2), the slope of the photocurrent gets reversed, too (see Fig. 6). The data are presented for room temperature and linearly polarized radiation with $\mathbf{e} \parallel x$. For this geometry, the MPGE current $j_x^{\text{MPGE}}/I = (S_1 + S_2)B_y + S_5B_z$ is phenomenologically determined by the coupling of the x -component of the current polar vector with components of the axial vector of the magnetic field, because $|e_x|^2$ is an invariant in (110)-grown structure. From the point of view of the phenomenological theory this situation is similar to the case of unpolarized radiation. Due to the symmetry arguments, presented above, the MPGE current for an in-plane \mathbf{B} -field is only proportional to the SIA coefficient. To check this, we rotated the sample by 90 degree so that the \mathbf{B} -field is oriented along x and the current is measured along the y -axis. In this geometry we detected a signal of the same magnitude and polarization dependence as before. This proves the axial symmetry of the signal expected for SIA contribution. Our observations also demonstrate that the position of the doping layer can be effectively used for tuning the structure asymmetry strength. In particular, the absence of the photocurrent for the in-plane magnetic field in sample E indicates that the QW is highly symmetric and lacks the structure asymmetry. The opposite sign of the MPGE observed for samples B and C having the same QW width demonstrates that the sign of $(S_1 + S_2)$ can be inverted by putting the doping layer to the other side of the QW.

The experiments discussed above are presented for

room temperature. However, all experimental features, such as magnetic field and polarization dependences, persist at least down to liquid helium temperature. Figure 7 shows the temperature dependence for the photocurrent in response to the radiation with $\lambda = 148\mu\text{m}$ for an in-plane magnetic field B_y . The data show that cooling the sample results in a significant increase of the photocurrent strength. We note that a similar temperature dependence for magnetic-field-induced photocurrents has been previously reported for (001)-oriented GaAs QWs and attributed to the conversion of pure spin currents, generated by THz radiation, into an electric current due to the equilibrium spin orientation caused by the Zeeman spin splitting¹³. The observation of a substantial MPGE response at low temperature on the one hand allows the investigation of the temperature dependence of SIA and on the other hand increases the sensitivity of the method. Also at low temperatures we did not observe a MPGE signal for an in-plane magnetic field in sample E, demonstrating that the structure remains symmetric. This is an important result in respect to a recent work on gate-dependent Kerr measurements, where surprisingly a large temperature dependence of SIA has been reported^{19,20}.

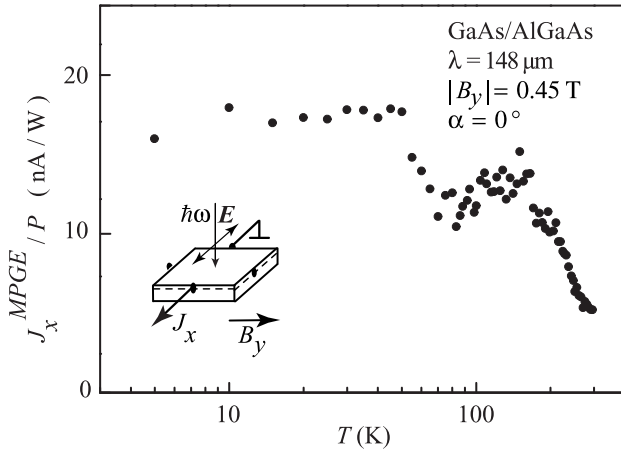


FIG. 7: Temperature dependence of the transverse magnetic field induced photocurrent J_x^{MPGE} . Data are obtained at an in-plane magnetic field of $|B_y| = 0.6\text{ T}$ and radiation with $P \sim 10\text{ kW}$ polarized along x .

Equations (2) and (8) show that for a magnetic field oriented perpendicular to the quantum well plane, the MPGE is allowed for both symmetrical and asymmetrical structures. The MPGE photocurrent for B_z is indeed observed for all samples. While no MPGE is observed for in-plane magnetic field in sample E, a sizable effect is detected for \mathbf{B} applied normal to the QW plane, see Fig. (8). The signals observed for an out-of-plane B_z field stem from the BIA term [see Eq. (8)]. Hence, measurement of the MPGE gives us an experimental handle to analyze the inversion asymmetry in (110)-oriented structures. Figure 9 shows the polarization dependence of the photocurrent detected in the single heterojunction, sample A, being in good agreement with Eq. (2).

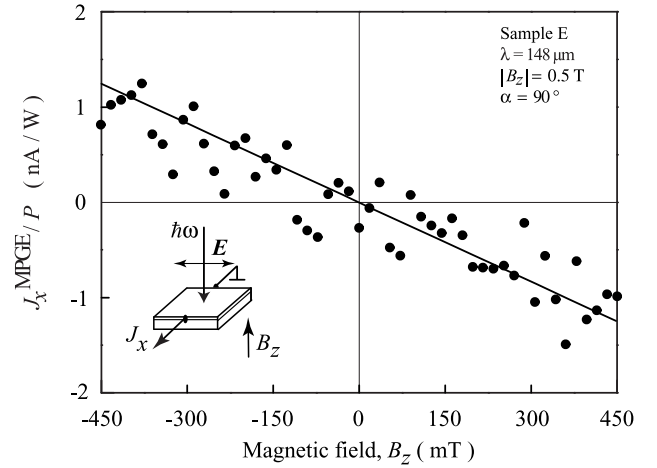


FIG. 8: Magnetic field dependences of the photocurrent J_x for sample E measured for the radiation polarized along x and a magnetic field perpendicular to the QWs. The magnetic field independent background discussed in the last section is subtracted.

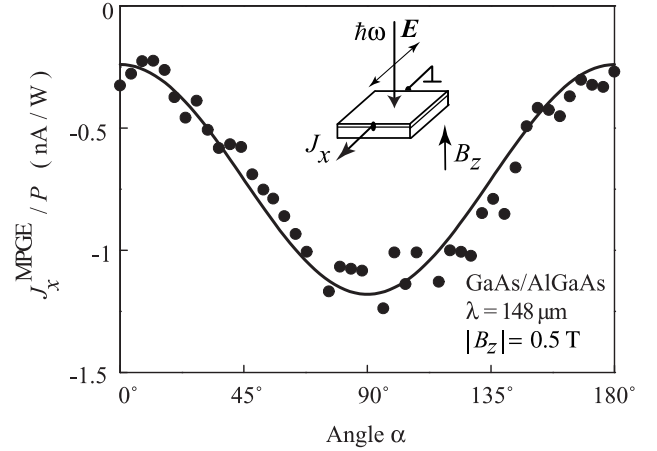


FIG. 9: Photocurrent J_x^{MPGE} as a function of angle α measured at normal incidence for a magnetic field perpendicular to the QWs. Photocurrent is excited by linearly polarized radiation with wavelength $\lambda = 148\mu\text{m}$ and power $P \sim 5\text{ kW}$. Full lines are fits to Eqs. (2). The inset shows the experimental geometry.

V. TIME-RESOLVED EXPERIMENTS

The structure inversion asymmetry determines the Rashba spin splitting and therefore controls the D'yakonov-Perel' (DP) relaxation^{7,8} for spins aligned along the z direction. Any variation of SIA, e.g., due to asymmetric doping, should result in a variation of the spin relaxation time. To directly demonstrate this connection, we compare spin relaxation rates measured in the symmetrically doped QW, sample E, and the asymmetrically doped QW, sample B. In the previous section, the potential profiles of samples E and B were identified via the MPGE indeed as symmetric and asymmet-

ric, respectively. We extract the spin lifetime τ_s from time-resolved Kerr rotation (TRKR).

We first discuss the spin lifetime in both, the symmetrically-grown sample E and the asymmetric sample B, as a function of the excitation density. Figure 10 shows two normalized TRKR traces measured on sample E at 4 K, using high and low excitation densities. At zero time delay, the pump pulse creates spin-polarized photocarriers, resulting in a maximum Kerr signal. This signal partially decays very rapidly within the first few picoseconds, then the decay becomes much slower. We attribute this first, rapid decay to the spin relaxation of the photogenerated holes, which typically lose their spin orientation within a few picoseconds in QWs²¹. We attribute the slower decay to the spin relaxation and recombination of the photogenerated electrons. It is clearly visible from the traces that the Kerr signal, and with it the electron spin polarization, decays more rapidly at higher excitation density.

The inset of Fig. 10 shows this increase of the spin lifetime for a reduction of the excitation density in sample E for a wide range of data. The spin lifetime in the asymmetric sample B, however, shows a different dependence on the excitation density: it is largest at the highest excitation density used in the measurements, then first decreases by about 30 percent as the excitation density is reduced. At lower excitation density, a slight increase is observed. Two factors may contribute to the marked increase of the spin lifetime with reduced excitation density in sample E:

First, the measured Kerr signal is proportional to the spin polarization within the sample. In undoped samples, a spin polarization may only persist during the lifetime of the generated photocarriers. Therefore, in samples where electron spin relaxation is slow compared to photocarrier recombination, the decay of the Kerr signal will reflect the lifetime of the photocarriers. In n-doped samples, like our structures, however, an electron spin polarization may remain after photocarrier recombination, as photogenerated holes partially recombine with unpolarized, resident electrons. The Kerr signal will therefore reflect a combination of electron spin relaxation and photocarrier recombination. If the excitation density is very low compared to the doping concentration within the sample, electron spin relaxation will dominate the decay of the Kerr signal, for high excitation density, the photocarrier recombination will increase the observed decay rate of the Kerr signal.

Second, the DP mechanism, which typically dominates the electron spin relaxation in GaAs QWs, is suppressed for spins aligned along the growth direction in the symmetrically-grown sample E. In its absence, other spin relaxation mechanisms become relevant. For low sample temperatures, we need to consider the Bir-Aronov-Pikus (BAP) mechanism. It describes the spin relaxation of electrons via their interaction with (unpolarized) holes. The strength of the BAP mechanism scales with the density of the photocreated holes, a reduction of the

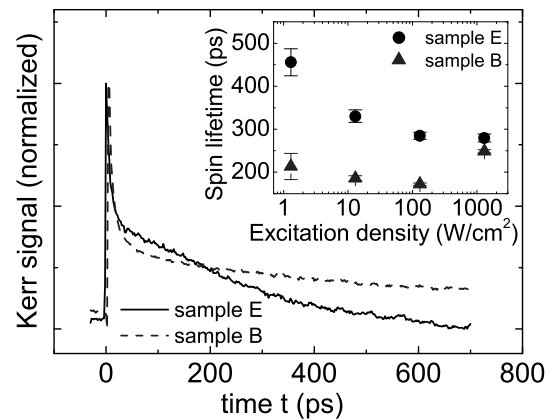


FIG. 10: Normalized TRKR traces measured on sample E at 4 K, with high (1300 W/cm², black line) and low (1 W/cm², red dotted line) excitation density. The inset shows the spin lifetime as a function of the excitation density at 4 K for samples E (black dots) and B (red triangles).

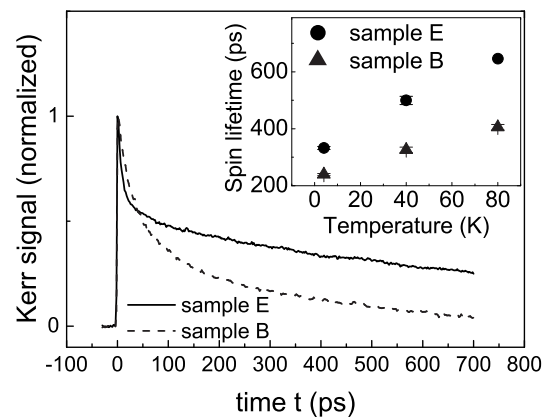


FIG. 11: Normalized TRKR traces measured on samples E (black line) and B (red dotted line) at 40 K with high excitation density. The inset shows the spin lifetime as a function of the sample temperature for samples E (black dots) and B (red triangles).

excitation density will therefore decrease its influence. Recent spin noise spectroscopy measurements²² demonstrate that the BAP mechanism strongly reduces the observed spin lifetime in (110)-grown QW systems, which may reach values above 20 ns in the absence of photogenerated holes.

From the excitation-density-dependent data, we may conclude that in sample B, the spin relaxation is dominated by the DP mechanism, as the asymmetric growth leads to SIA and a corresponding Rashba spin splitting. The BAP mechanism is, by comparison, far less important for spin relaxation in this sample, therefore the reduction of the photogenerated hole density does not significantly increase the spin lifetime. The increase of the spin lifetime for the highest excitation density may be due to the increase in initial spin polarization, as observed previously in (001)-grown 2D electron systems²³.

Next, we investigate the spin lifetime in sample B and E as a function of the sample temperature. Figure 11 shows two normalized TRKR traces measured on these samples at 40 K, using a high excitation density. Both samples show a partial decay of the Kerr signal during the first few ps after excitation, which we again attribute to the spin relaxation of photoexcited holes. After this initial decay, the Kerr signal of sample E decays significantly more slowly than that of sample B. The inset in Fig. 11 shows the spin lifetimes of the two samples as a function of temperature. These spin lifetimes were determined by an exponential fit to the TRKR traces starting at $t=200$ ps in order to exclude the hole spin relaxation. We note that the symmetrically-grown sample E shows a spin lifetime which is about 50 percent larger than that of sample B, within the whole temperature range investigated here. This observation clearly confirms our interpretation that in the symmetrically-grown sample E, the Rashba spin-orbit field is absent, and spin relaxation via the DP mechanism is suppressed, while it is still present, and dominates the spin relaxation, in the asymmetric sample B. All the temperature-dependent measurements were performed at rather high excitation density (130 W/cm^2), therefore, the measured spin lifetime for sample E is significantly lower than the intrinsic limit in the absence of photocarriers. As the inset in Fig. 11 shows, the spin lifetime in both samples increases monotonically with increasing temperature. We can identify two factors, which contribute to this increase:

(i) At higher excitation density, the TRKR decay is increased by photocarrier recombination. In order to study the temperature dependence of the photocarrier lifetime, we performed TRPL measurements on sample E as a function of temperature. Figure 12 shows normalized, spectrally averaged TRPL traces measured on sample E at 4 K and 125 K. After pulsed excitation at $t=0$ ns, the low-temperature TRPL trace shows an increase of the PL intensity within the first 150 ps, then the PL intensity decreases monotonically. This behavior is typical for nonresonant excitation of a QW at low temperatures⁷, as the photoexcited electrons and holes first have to reduce their momenta via scattering to enter the so-called light cone²⁴ before they may recombine radiatively. The trace taken at 125 K does not show this initial increase, but monotonically decreases after excitation. At these elevated temperatures, carrier-phonon scattering is much more pronounced, allowing for faster scattering of the photoexcited carriers into and out of the light cone. The latter effect leads to an increase of the PL lifetime as the temperature is increased. The photocarrier lifetime is extracted from the TRPL data by an exponential fit to the TRPL traces starting at $t=0.5$ ns in order to exclude the influence of initial thermalization and carrier-phonon scattering. The inset in Fig. 12 shows this photocarrier lifetime as a function of temperature. It increases by about 90 percent as the sample temperature is raised from 4 K to 125 K, then decreases again slightly. In the temperature range where we have

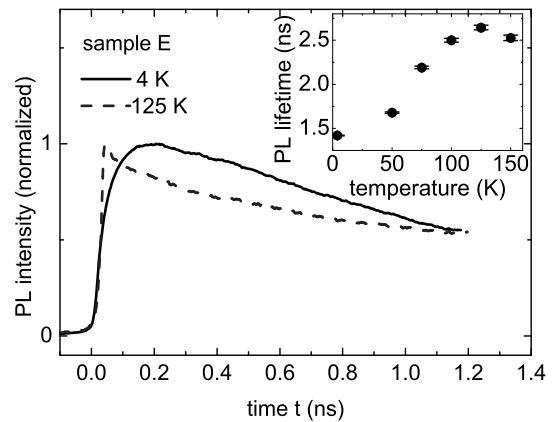


FIG. 12: Spectrally integrated TRPL traces measured on sample E for 4 K (black line) and 125 K (red dotted line). The inset shows the PL lifetime as a function of temperature for sample E.

studied the spin lifetime in our samples, the photocarrier lifetime increases monotonically, therefore reducing the TRKR decay via photocarrier recombination. We note that the photocarrier lifetime after near-resonant excitation is typically shorter than that observed after nonresonant excitation. Therefore, the TRPL data give only a qualitative indication of the photocarrier lifetime under conditions of near-resonant excitation.

(ii) The BAP mechanism, which limits the spin lifetime, especially in the symmetrically-grown sample E, may become less important in our structures as the sample temperature is increased. The temperature dependence of the BAP mechanism in QWs was recently investigated theoretically by Zhou et al.²⁵ using the kinetic spin-Bloch equations approach. In their model, they observe an increase of the BAP mechanism as the sample temperature is raised, which is in contrast to our observations. One possible explanation for this contradiction may be the experimental conditions: in the TRKR measurements, the holes are created locally by the pump beam. With increasing temperature, the spatial overlap between electrons and holes is reduced³, leading to the observed increase in photocarrier lifetime and spin lifetime.

VI. PHOTOCURRENTS AT ZERO MAGNETIC FIELD

Investigating the MPGE one should take into account that in (110)-oriented structures optical excitation may generate other photocurrents at normal incidence, even for zero magnetic field. The MPGE, however, can easily be extracted from the total photocurrent by treating the data after Eq. (10). Indeed, only the MPGE being odd in B , changes its direction when the magnetic field direction is inverted. In the infrared/terahertz spectral range there can be two sources of photocurrents at homo-

geneous excitation which occur simultaneously and may be of the same order of magnitude as the MPGE. These are the linear and circular photogalvanic effects and the photon drag effect^{11,12}. Our experiments demonstrated that in the investigated samples the photocurrent at zero magnetic field is in most cases caused by the linear photogalvanic effect. The photocurrent is observed in both, x and y directions for linearly as well as for elliptically polarized radiation. Figure 13 shows the photocurrent detected in sample A for room temperature and zero magnetic field as a function of the azimuth angle of linear polarization (Fig. 13a) and radiation helicity (Fig. 13b). The latter plot reveals that in x direction, being perpendicular to the mirror reflection plane m_1 , the circular photogalvanic effect overweighs the linear photogalvanic effect. The data are in a good agreement with Eqs. (9).

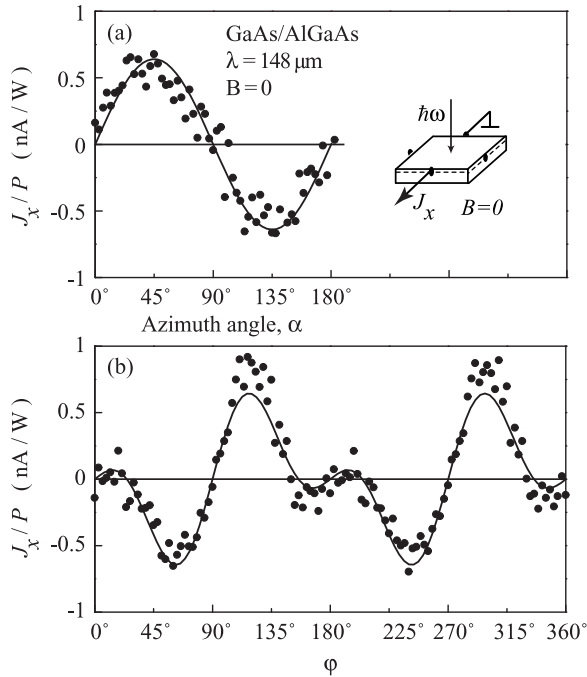


FIG. 13: Photocurrent, measured at zero magnetic field along the crystallographic direction $x \parallel [1\bar{1}0]$ as a function of (a) azimuth angle α and (b) the angle φ . The photocurrent is excited by radiation with wavelength $\lambda = 148 \mu\text{m}$ and power $P \sim 5 \text{ kW}$. Full lines are fits to Eqs. (9). The inset shows the experimental geometry.

VII. SUMMARY

We have studied photocurrents in n -doped zinc-blende based (110)-grown QWs generated by Drude absorption

of normally incident terahertz radiation in the presence of an in-plane and out of plane magnetic field. The results agree with the phenomenological description based on the symmetry. The observation of polarization-dependent as well as polarization-independent photocurrents reveal that both, an asymmetry of photoexcitation and asymmetry of energy relaxation contribute substantially to the MPGE in (110)-grown QWs. We show that the MPGE provides a tool to probe the degree of the structural inversion asymmetry which defines the spin relaxation in (110)-grown quantum wells. Parallel to the MPGE experiments, we also investigated spin relaxation applying time-resolved Kerr rotation and luminescence. As an important result of all our measurements we obtained a zero current response in the in-plane magnetic field and the longest spin relaxation time from the symmetrically doped QWs, which set an upper limit of spin dephasing in GaAs QWs. This is in contrast to (001)-grown structures, where such a growth procedure results in a substantial SIA^{26,27}. This essential difference stems most likely from increased segregation at high growth temperatures, and, subsequently, the diffusion length of dopant atoms. Indeed, the growth temperature of high-quality (001)-oriented QWs is higher than 600°C , while (110)-structures are grown at 480°C ²⁸. High growth temperature of (001)-oriented heterostructures leads to substantial dopant migration and results in structure asymmetry of nominally symmetrically doped QWs. The investigation of the MPGE, in particular the sign inversion by reversing of structural asymmetry and the zero current response in MPGE of symmetrical structures, provides an effective access to study the symmetry of (110)-oriented QWs. The observed rise of the photocurrent strength with decreasing temperature demonstrates that the MPGE can be applied to investigate the inversion asymmetry in a wide range of temperatures including technologically important room temperature, where many methods, like weak localization, or polarized luminescence, can not be used. In summary our photocurrent measurements provide the necessary feedback to reliably grow structures with long spin relaxation times.

We thank E.L. Ivchenko and M.W. Wu for fruitful discussion, as well as V. Lechner and S. Stachel. The financial support by the DFG and RFBR is gratefully acknowledge.

¹ Y. Ohno *et al.*, Phys. Rev. Lett. **83**, 4196 (1999).

² O. Z. Karimov *et al.*, Phys. Rev. Lett. **91**, 246601 (2003).

³ S. Döhrmann *et al.*, Phys. Rev. Lett. **93**, 147405 (2004).

⁴ K. C. Hall *et al.*, Appl. Phys. Lett. **86**, 202114 (2005).

- ⁵ M. I. D'yakonov and V. Yu. Kachorovskii, Sov. Phys. Semicond. **20**, 110 (1986).
- ⁶ Y.A. Bychkov, and E.I. Rashba, Pis'ma ZhETF **39**, 66 (1984) [Sov. JETP Lett. **39**, 78 (1984)].
- ⁷ *Spin Physics in Semiconductors*, ed. M. I. Dyakonov (Springer, Berlin 2008).
- ⁸ J. Fabian *et al.*, *Semiconductor Spintronics* review, Acta Phys. Slov. **57**, 565 (2007).
- ⁹ V.V. Bel'kov *et al.*, Phys. Rev. Lett. **100**, 176806 (2008).
- ¹⁰ V.V. Bel'kov, and S.D. Ganichev, review in special issue of Semicond. Sci. Technol. **23**, 114003 (2008).
- ¹¹ E. L. Ivchenko, *Optical Spectroscopy of Semiconductor Nanostructures* (Alpha Science Int., Harrow, 2005).
- ¹² S. D. Ganichev and W. Prettl, *Intense Terahertz Excitation of Semiconductors* (Oxford Univ. Press, 2006).
- ¹³ S. D. Ganichev *et al.*, *Nature Physics* **2**, 609 (2006).
- ¹⁴ S.A. Tarasenko, Phys. Rev. B **77**, 085328 (2008).
- ¹⁵ V. V. Bel'kov *et al.*, J. Phys.: Condens. Matter **17**, 3405 (2005).
- ¹⁶ Note that C_{2v} point group symmetry also describes the (001)-grown asymmetric structures. In this case, however, both mirror reflection planes are perpendicular to the interface plane.
- ¹⁷ V.A. Shalygin *et al.*, JETP Lett. **84**, 570 (2006).
- ¹⁸ S.D. Ganichev *et al.*, *Nature* (London) **417**, 153 (2002).
- ¹⁹ P. S. Eldridge *et al.*, arXiv:0807.4845 (2008).
- ²⁰ P. S. Eldridge *et al.*, Phys. Rev. B **77**, 125344 (2008).
- ²¹ T. C. Damen *et al.*, Phys. Rev. Lett. **67**, 3432 (1991).
- ²² G. M. Müller *et al.*, Phys. Rev. Lett. **101**, 206601 (2008).
- ²³ D. Stich *et al.*, Phys. Rev. Lett. **98**, 176401 (2007).
- ²⁴ D. Sanvitto *et al.*, Phys. Rev. B **62**, 13294 (2000).
- ²⁵ J. Zhou and M. W. Wu, Phys. Rev. B **77**, 075318 (2008).
- ²⁶ S. Giglberger *et al.*, Phys. Rev. B **75**, 035327 (2007).
- ²⁷ V. Lechner *et al.*, arXiv cond-mat 0903.1232.
- ²⁸ L. Pfeiffer *et al.*, Appl. Phys. Lett. **56**, 1697 (1990).